ARTICLE   OPEN

Check for updates

Realization of practical eightfold fermions and fourfold van Hove singularity in TaCo$_2$Te$_2$

Hongtao Rong[1,11], Zhenqiao Huang [1,2,11], Xin Zhang[3,4,11], Shiv Kumar[5,11], Fayuang Zhang[1], Chengcheng Zhang[1], Yuan Wang[1], Zhanyang Hao[1], Yongqing Cai[1], Le Wang[1], Cai Liu[1], Xiaoming Ma[1], Shu Guo[1], Bing Shen [6], Yi Liu[7], Shengtao Cui[7], Kenya Shimada [5], Quansheng Wu[8,9], Junhao Lin[1], Yugui Yao [3,4], Zhiwei Wang [3,4,10✉], Hu Xu[1✉] and Chaoyu Chen [1✉]

Space groups describing the symmetry of lattice structure allow the emergence of fermionic quasiparticles with various degeneracy in the band structure. Theoretical efforts have predicted many materials hosting fermions with the highest degeneracy, i.e., eightfold fermions, yet lacking experimental realization. Here, we explore the band degeneracies in TaCo$_2$Te$_2$ crystals. Through systematic experimental and theoretical analyses, we establish TaCo$_2$Te$_2$ as a nonsymmorphic crystal with negligible spin–orbit coupling (SOC) and long-range magnetic order. These critical properties guarantee the realization of practical eightfold fermions and fourfold van Hove singularity, as directly observed by photoemission spectroscopy. TaCo$_2$Te$_2$ serves as a topological quantum critical platform, which can be tuned into various magnetic, topologically trivial, and nontrivial phases by adding strain, magnetic field, or SOC. The latter is demonstrated by our first-principles calculations, which show that enhancing SOC in TaCo$_2$Te$_2$ will promote the experimental observation of bulk hourglass fermions. Our results establish TaCo$_2$Te$_2$ as a platform to explore the interplay between symmetry and band topology.

INTRODUCTION

It has been an eternal theme in condensed matter physics to explore emerging low-energy elementary excitations from many-body interactions and/or symmetry constraints. In analog to high-energy physics, where the Poincaré symmetry allows relativistic massless Weyl and Dirac fermions, in condensed matter physics, Weyl and Dirac-type low-energy quasiparticle excitations have been realized based on materials like graphene[1,2], topological insulator[3–6], and topological semimetals[7–13]. At zero momentum, Weyl and Dirac fermions are twofold and fourfold degenerate, respectively. Moreover, as subgroups of the Poincaré symmetry, the 230 space groups in condensed matter physics impose fewer constraints on the allowed types of fermions. Fermionic quasi-particles beyond high-energy physics, including threefold, sixfold, and eightfold fermions, can emerge as band degeneracy[14–26]. Experimental exploration of such band degeneracy represents a major and yet-to-be-accomplished task.

In Table 1, the spectroscopic observation of fermionic excitations as band degeneracy in crystalline materials is summarized according to the band degeneracy g and the order of dispersion n. According to theoretical analysis, there exist cubic ($n = 3$) Weyl and Dirac fermions[21,23] yet lack experimental observation. Quadratic ($n = 2$) Dirac and sixfold fermions have been observed directly by angle-resolved photoemission spectroscopy (ARPES) in α-Sn[27] and PdSb$_2$[28–30], respectively. Besides, all the experimentally realized fermionic quasiparticles are of linear dispersion ($n = 1$)

with band degeneracy $g = 2, 3, 4, 6$. However, for quasiparticles with the highest band degeneracy, i.e., eightfold fermions, despite its theoretical prediction based on space groups 130, 135, 218, 220, 222, 223, 230[15,19,21,24,25], the spectroscopic observation is still missing. This is particularly due to the difficulty in growing or handling the candidate materials[31–33]. Our approach to overcome this is to seek materials with negligible spin–orbit coupling (SOC) effect, which loses symmetry constraints and expands the space group selection.

In this work, we report the practical realization of eightfold fermion in a nonsymmorphic (space group 62) crystal TaCo$_2$Te$_2$. Magnetic property measurements reveal no signature of long-range magnetic order despite the existence of Co atoms. ARPES measurement revealed a double Dirac cone (DDC) feature at the Brillouin zone (BZ) $\overline{X}$ point. Density functional theory (DFT) analysis prove this feature as an eightfold degenerate node at the S point of bulk BZ, protected by the combination of crystalline and time-reversal symmetry. The inclusion of SOC only opens a negligible gap, rendering a practical realization of eightfold fermions. Such symmetry combination also protects a fourfold (robust against SOC) van Hove singularity (VHS) at Z close to the Fermi level (E_F), which represents a type of VHS beyond the recent classifications of high-order VHSs[34,35]. Both the eightfold fermion and fourfold VHS have been directly observed by ARPES. These magnetic and electronic properties establish TaCo$_2$Te$_2$ as a topological quantum critical platform that can be tuned into various magnetic, topologically trivial, or nontrivial phases[15,19], say, by inducing

[1]Shenzhen Institute for Quantum Science and Engineering (SIQSE) and Department of Physics, Southern University of Science and Technology (SUSTech), 518055 Shenzhen, China. [2]Department of Physics, The Hong Kong University of Science and Technology, Clear Water Bay, Hong Kong, China. [3]Centre for Quantum Physics, Key Laboratory of Advanced Optoelectronic Quantum Architecture and Measurement, School of Physics, Beijing Institute of Technology, 100081 Beijing, China. [4]Beijing Key Lab of Nanophotonics and Ultrafine Optoelectronic Systems, Beijing Institute of Technology, 10008 Beijing, China. [5]Hiroshima Synchrotron Radiation Centre, Hiroshima University, 739-0046 Higashi-Hiroshima, Hiroshima, Japan. [6]School of Physics, Sun Yat-Sen University, 510275 Guangzhou, China. [7]National Synchrotron Radiation Laboratory, University of Science and Technology of China, 230029 Hefei, Anhui, China. [8]Beijing National Laboratory for Condensed Matter Physics, and Institute of Physics, Chinese Academy of Sciences, 100190 Beijing, China. [9]University of Chinese Academy of Sciences, 100049 Beijing, China. [10]Material Science Center, Yangtze Delta Region Academy of Beijing Institute of Technology, 314011 Jiaxing, China. [11]These authors contributed equally: Hongtao Rong, Zhenqiao Huang, Xin Zhang, Shiv Kumar. ✉email: zhiweiwang@bit.edu.cn; xuh@sustech.edu.cn; chency@sustech.edu.cn

Table 1. Experimental observation of different types of fermions in material families.

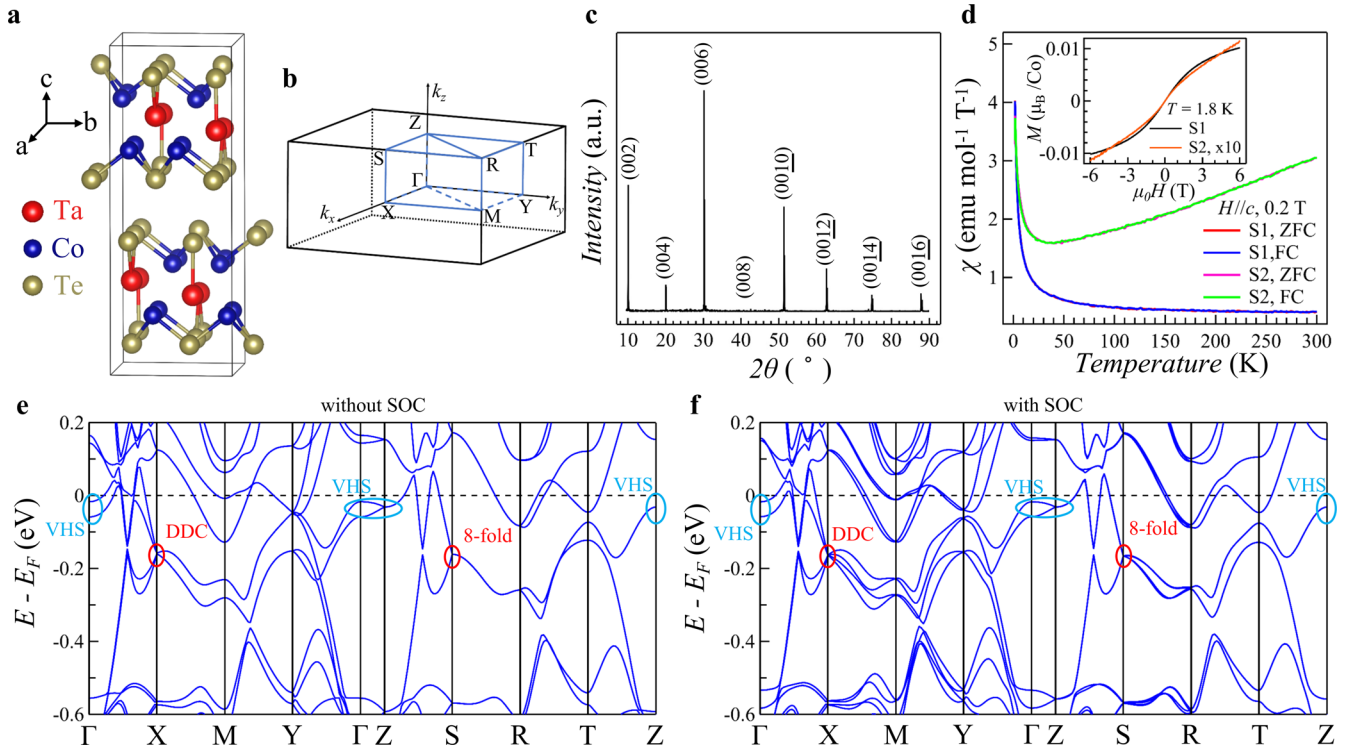| Order of dispersion n	Band degeneracy g					
	2	3	4	6	8	
1	TaAs[7–11], MoTe$_2$[52–54], LaAlGe[55], TaIrTe$_4$[56], YbMnBi$_2$[57], Co$_2$MnGa[58], Co$_3$Sn$_2$S$_2$[59]	MoP[60,61]	Na$_3$Bi[10,13] Cd$_3$As$_2$[12] PtSe$_2$[62–67]	CoSi[68–73] PdBiSe[74]	TaCo$_2$Te$_2$ This work	
2	? (awaiting experimental proof)	?	α-Sn[27]	PdSb$_2$[28–30]	Forbidden	
3	?	Forbidden	?	Forbidden	Forbidden	

Fig. 1 Eightfold fermions and fourfold VHS in nonsymmorphic TaCo$_2$Te$_2$ with negligible magnetic order. a Crystal structure of TaCo$_2$Te$_2$. **b** Three-dimensional BZ of TaCo$_2$Te$_2$. **c** Single-crystal X-ray diffraction (XRD) result taken at 300 K. **d** Zero-field-cooled (ZFC) and field-cooled (FC) magnetic susceptibility (χ) vs. temperature (T) for magnetic field $H = 0.2$ T parallel to the c axis. Inset: Field-dependent magnetization (M) at 1.8 K. **e, f** DFT calculated dispersions along the high-symmetry path without considering SOC (**e**) and with SOC (**f**).

magnetism, SOC, symmetry breaking via chemical, strain, or band engineering. As an example, we use DFT calculation to prove that enhancement of SOC would increase the band pair splitting of bulk hourglass fermions hosted by TaCo$_2$Te$_2$ and make the ARPES observation of such band features feasible. These results suggest TaCo$_2$Te$_2$ as a platform to explore the interplay between symmetry and band topology.

RESULTS

Basic properties of TaCo$_2$Te$_2$

TaCo$_2$Te$_2$ crystallizes in an orthorhombic structure[36]. Using single-crystal X-ray diffraction (SCXRD), we determine its lattice structure as lattice constants α = 6.6116 Å, b = 6.5735 Å, c = 17.783 Å in space group 62 (*Pmcn*). The corresponding BZ is shown in Fig. 1b. The crystallinity of as-grown single crystals was examined by XRD. As shown in Fig. 1c, all the diffraction peaks can be well indexed by the (00*l*) reflections with c = 17.783 Å. The magnetic property of TaCo$_2$Te$_2$ is shown in Fig. 1d. First, no order behavior can be observed from $\chi - T$ measurement, indicating the absence

of magnetic order in the current temperature region. Between 100 and 300 K, the slope of $\chi - T$ curves can be positive or negative depending on samples, neither of which can be fitted by Curie–Weiss law, indicating extrinsic origin. Second, the value of χ in TaCo$_2$Te$_2$ is 3 orders of magnitude lower compared to typical cobalt compound Co$_3$Sn$_2$S$_2$[37,38], suggesting negligible Co moment. Third, the field-dependent magnetization ($M - H$) curves show no signs of saturation or hysteresis. All the above magnetic properties enable us to omit the magnetism of TaCo$_2$Te$_2$ in the following electronic structure study.

Calculated band structures of TaCo$_2$Te$_2$

Figure 1e, f shows the band structure of TaCo$_2$Te$_2$ along the high-symmetry path calculated by DFT without and with considering SOC, respectively. Due to the experimentally observed Fermi level being about 50 meV lower than the theoretical Fermi level, we adjust the Fermi level and use the experimentally observed Fermi level as a reference in Fig. 1e, f. Two exotic features in the $k_z = 0$ plane ($\Gamma - X - M - Y - \Gamma$ plane) are noticeable. The first one is a DDC feature ($\sim -0.17 eV$) at X point (highlighted by red ellipses).
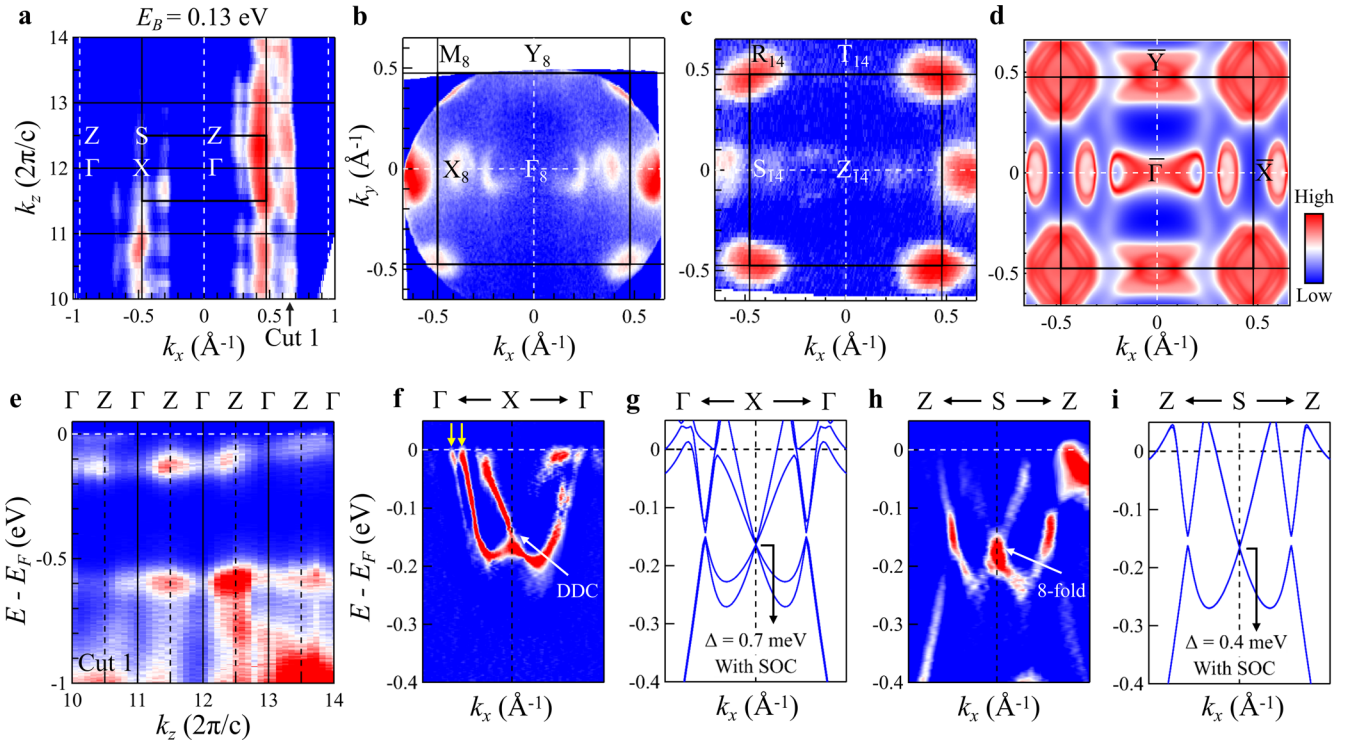
Fig. 2 Observation of practical eightfold fermions in TaCo₂Te₂. a Integrated photoemission intensity maps in the $k_x - k_z$ plane taken at $E_B = 0.13$ eV measured by varying photon energy. **b, c** Fermi surface in the $k_x - k_y$ plane measured with photon energies 24 eV and 90 eV, respectively. **d** Fermi surface calculated by DFT with projection to the $k_x - k_y$ plane. **e** The band dispersion along the k_z direction at $k_x = 0.67$ Å^{-1} as shown in (**a**) Cut1. **f–i** ARPES measured spectra (second derivative plot) and corresponding DFT calculated dispersions along high-symmetry paths with SOC.

Figure 2g shows that this DDC has two fourfold degenerate points separated by a Dirac gap $\sim 0.7 meV$. The second one is a double VHS feature close to E_F at Γ point (highlighted by blue ellipses). Along Γ − X direction they are electron pockets centered at Γ and crossing E_F, while along Γ − Y they are hole-like, yielding two saddle point VHSs.

When moving to $k_z = \pi$ plane (Z − S − R − T − Z plane), the energy splitting between band pairs decreases and even vanishes, resulting in doubled band degeneracy. The DDC feature at X merges into a single, fourfold Dirac cone with a gapless, eightfold degenerate point at S (Fig. 2h, i). This eightfold fermion is symmetry-protected without SOC, determined by the projective irreducible representations (IReps) of the little group at S. Since the system is nonmagnetic without considering SOC, we only need to consider single-valued IReps. The nonsymmorphic group $Pmcn$ has higher dimension IReps at the boundary of the first BZ[39]. At S, the little group has two two-dimension IReps, which are conjugated to each other. Due to the time-reversal symmetry, the two conjugated IReps will become a four-dimension IRep through the direct sum. Moreover, since the SOC here is negligible, we first consider a system without SOC. In this case, the spin space has SU(2) symmetry protecting the spin degeneracy. Therefore, the band at the S point is eightfold degenerate. On the other hand, when considering SOC, the degeneracy will be determined by the double-valued projective IReps of the little group, and the SU(2) symmetry will be broken. Although the double-valued IReps of the little group at S also include a four-dimension IRep, the time reversal cannot lead to eightfold degeneracy[15,19]. Therefore, SOC will generally open a gap at S. But the following ARPES measurement (unresolvable) and DFT analysis ($\sim 0.4 meV$) both manifest that this SOC-induced gap is negligible.

Besides, the double VHSs at Γ merge into one single VHS at Z, forming a fourfold VHS, robust against SOC. First, Z is invariant

under inversion symmetry P and a glide mirror $\tilde{M}_x : (x, y, z) \rightarrow (-x, y + \frac{1}{2}, z + \frac{1}{2})$. In this case, if a Bloch state $|u\rangle$ is an eigenstate of $\tilde{M}_x$ with eigenvalue g_x, there is another state of the system $P|u\rangle$. Moreover, because of the fractional translation of $\tilde{M}_x$, the two operators are anticommutative, $\{P, \tilde{M}_x\} = 0$, which gives $\tilde{M}_x P|u\rangle = -P\tilde{M}_x|u\rangle = -g_x P|u\rangle$. Thus, $|u\rangle$ and $P|u\rangle$ must be linearly independent for their opposite eigenvalues. Then, since Z is a time-reversal invariant momentum and the time-reversal operator T has $T^2 = -1$, the band at this point has a Kramer double degeneracy. Therefore, for the states $|u\rangle$ and $P|u\rangle$, there must be linearly independent states $T|u\rangle$ and $TP|u\rangle$ having the same energy. Because $PT = TP$ here, $TP|u\rangle$ is equal to $PT|u\rangle$. So, the independence of $T|u\rangle$ and $TP|u\rangle$ can also be argued by the anticommutation relation. Furthermore, the Z point is also invariant under the combination of time-reversal and inversion symmetries TP with $(TP)^2 = -1$. Thus, $TP|u\rangle$ is another Kramer-like double degenerate state of $|u\rangle$ at Z. Therefore, for any eigenstates $|u\rangle$ of $\tilde{M}_x$ with momentum vector $(0, 0, \pi)$ in the crystal, there must be three linearly independent states $P|u\rangle$, $T|u\rangle$, and $TP|u\rangle$. Namely, the bands at Z are all fourfold degenerate.

Practical eightfold fermions in TaCo₂Te₂

Photon energy-dependent ARPES measurement shown in Fig. 2a presents a periodic pattern of spectral intensity in the $k_x - k_z$ plane taken at $E_B = 0.13$ eV, helping to define the high-symmetry points of Γ, Z, X, S, using lattice constant $c = 17.78$ Å and inner potential $V_0 = 13.5 eV$. Figure 2e shows the corresponding band dispersion along k_z direction at $k_x = 0.67$ Å^{-1}. Fermi surfaces mapped by ARPES at different k_z planes in Fig. 2b, c present features consistent with the DFT projection (Fig. 2d). Of particular interest are two elliptical features next to $\overline{X}$, which come from the DDC features along $\overline{Γ} - \overline{X} - \overline{Γ}$ direction. In Fig. 2f–i, we compare the ARPES measured DDC spectra along Γ − X − Γ and Z − S − Z to the DFT calculated
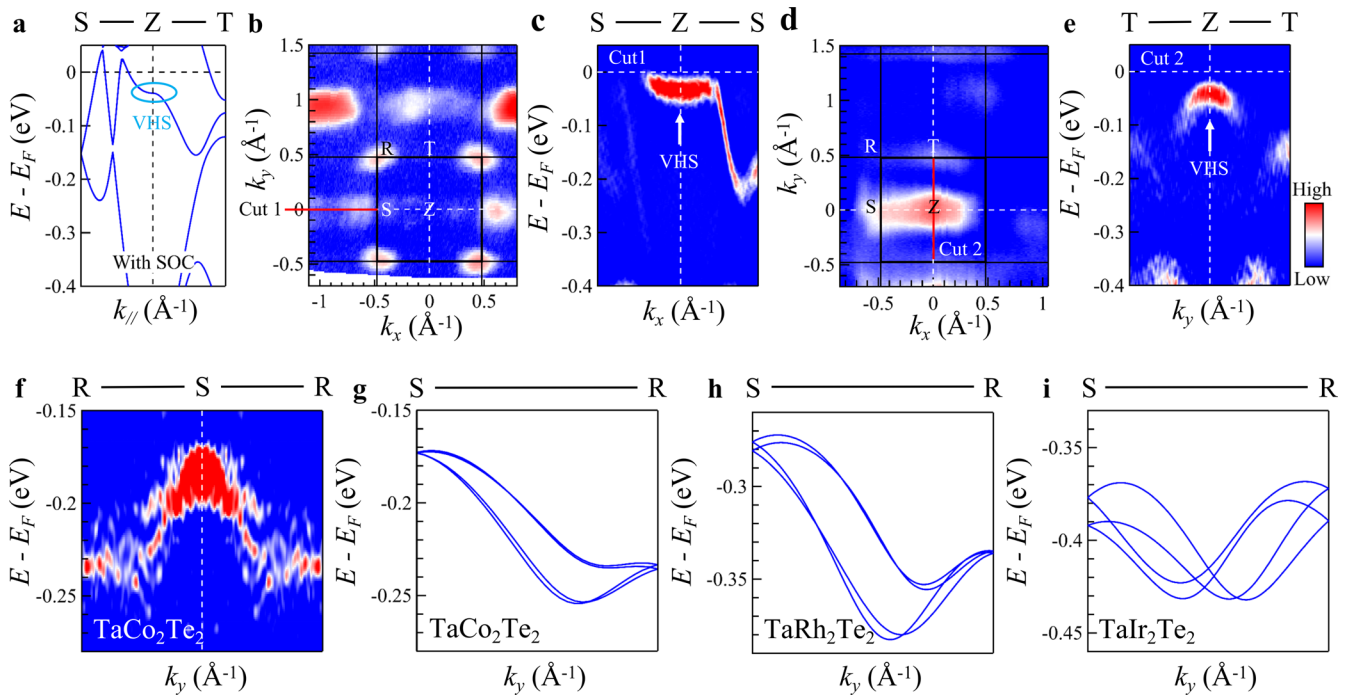
Fig. 3 Observation of fourfold VHSs in TaCo$_2$Te$_2$ and predicted realization of hourglass fermions in TaIr$_2$Te$_2$. a DFT calculated fourfold bands along $S - Z - T$. **b, d** Fermi surface in $k_x - k_y$ plane measured with photon energy $90 eV$, with the measurement plane defined by the incident light and emitted electrons parallel to $Z - S$ (**b**) and $Z - T$ (**d**) directions, respectively. **c, e** Second derivative ARPES spectra taken from the momentum cut indicated by red lines in (**b**) and (**d**), respectively. **f** Second derivative ARPES spectra showing the feature of hourglass fermion predicted in TaCo$_2$Te$_2$. **g–i** DFT predicted hourglass fermions.

ones. For the DDC feature centered at X, the band pair splitting can be clearly resolved in the second derivative plot and splitting bands are marked by yellow arrows shown in Fig. 2f (for details, see Supplementary Fig. 1a–c). It is noted that this splitting in ARPES spectra is more evident for the outer cones than the inner ones, probably resulting from the fact that the inner ones are more dispersed along k_z direction, and its projection into the $k_x - k_y$ plane may smear out its own splitting. According to the above symmetry analysis, moving to $k_z = \pi$ plane merges the DDC feature into a single but fourfold degenerate Dirac cone, with an eightfold degenerate Dirac point (as shown in Fig. 2i. For details, see Supplementary Fig. 1d–f). This is indeed observed in the ARPES spectral along $Z - S - Z$ direction, as shown in Fig. 2h. Compared to ARPES spectra along $\Gamma - X - \Gamma$, spectra along $Z - S - Z$ show the absence of band pair splitting and the presence of a degenerate point with enhanced spectral weight. These features clearly prove the fourfold band degeneracy and the existence of eightfold fermion. The SOC-induced gap ($\sim 0.4 meV$ according to DFT in Fig. 2i) is negligible compared to the breadth of observed bands in ARPES spectra (Fig. 2h).

Fourfold VHSs in TaCo$_2$Te$_2$

We then focus on the fourfold VHS at the Z point as shown in Fig. 3a. According to DFT, this VHS manifests itself as an electron pocket along $Z - S$ and a hole pocket along $Z - T$, thus as a saddle point with a divergent density of states. To measure the corresponding spectra, we first align the $Z - S$ direction parallel to the measurement plane and then make a Fermi surface mapping. As shown by the mapping in Fig. 3b, the spectral weight is heavily suppressed at Z in the first BZ due to the measurement geometry and orbital symmetry of the contributing electrons. So we chose the extended BZ to extract the cut along $S - Z - S$. As shown in Fig. 3c, ARPES spectra indeed present an electron-like pocket centered at Z with its minimum binding energy $\sim 32 meV$. Then the sample is rotated by $90°$ so that $Z - T$ is parallel to the

measurement plane. The ARPES spectra along $T - Z - T$ are extracted from the corresponding Fermi surface mapping (Fig. 3d). As shown in Fig. 3e, a hole-like pocket centered at Z can be resolved. Comparing Fig. 3c and e, it is found that the minimum of the electron pocket along $S - Z - S$ coincides with the maximum of the hole pocket along $T - Z - T$, being evidence of a saddle point. As our previous symmetry analysis has proven Z as a fourfold degenerate point, this saddle point is thus a fourfold degenerate VHS, which goes beyond the recent classifications of high-order VHSs[34,35]. In the energy-resolved density of states (DOS) plot, a significant DOS enhancement at the saddle point energy can be seen (for details, see Supplementary Fig. 2).

DISCUSSION

Combining magnetic, structural, and electronic structure experiments and calculations, we have proved that TaCo$_2$Te$_2$ shows topological quantum critical behaviors related to its magnetic and electronic properties. Chemical substitution or applying strain may change the valence state of Co atoms and introduce large magnetic moments so that long-range magnetic order and magnetic quantum critical points are expected (for details, see Supplementary Figs. 3–5). The negligible SOC leads to the practical realization of eightfold fermions, which, according to theoretical analysis[15,19], serves as a topological quantum critical point. Symmetry breaking via magnetic field or uniaxial strain may lead to various topologically trivial or nontrivial phases such as Dirac point, Weyl point, or nodal lines. The enhanced DOS by eightfold degeneracy and fourfold VHS also amplifies electron correlation, potentially resulting in various ordering instabilities and many-body interactions. Thus, we establish TaCo$_2$Te$_2$ as a conjoint topological and quantum critical platform with a handful of stimuli available to tune its physical properties.

We take SOC as an example of such a stimulus to theoretically demonstrate its tunability. As shown in Fig. 3g, the nonsymmorphic

symmetry guarantees band features hosting hourglass fermions[17] along S − R in TaCo$_2$Te$_2$, distinct from surface hourglass fermions as discussed in KHgSb[40], which are the surface states in a type of topological insulators[17]. The bulk hourglass fermion in our work is a nodal loop semimetal constructed by the hourglass crossing points in the glide-invariant plane of the BZ[41,42]. It has been shown that the nodal loop in the bulk can give rise to drumhead surface states with a split band at the sample surface where the nodal loop is projected on[43]. As shown in Fig. 3g, the predicted splitting between adjacent Dirac crossing is too small to be resolved in the ARPES spectra in Fig. 3f. Increasing the effect of SOC, e.g., via substituting Co with Rh or Ir, would increase the adjacent Dirac crossing splitting and promote the practical observation of hourglass fermion features by ARPES. This expectation is indeed true, as proved by our DFT calculation on the isostructural TaT_2Te$_2$, where T represents Co, Rh, and Ir (Supplementary Fig. 6). As shown in Fig. 3g–i, in the considered energy-momentum region always exists an hourglass fermion feature for all the three materials. With increasing SOC, the energy splitting between adjacent Dirac points increases from $\sim 3 meV$ in TaCo$_2$Te$_2$ to $\sim 15 meV$ in TaIr$_2$Te$_2$. The latter energy scale is comparable to the breadth of observed bands here, thus making the ARPES observation of hourglass fermions and the related drumhead surface states in TaIr$_2$Te$_2$ very promising. Our observation thus calls for further efforts to explore exotic states of matter and the interplay between symmetry and band topology based on the TaCo$_2$Te$_2$ family of materials.

METHODS

Sample growth and characterizations

High-quality TaCo$_2$Te$_2$ single crystals were synthesized using a chemical vapor transport method with I$_2$ as a transport agent. The mixture of Ta powder (purity 99.9%), Co pieces (99.99%), and Te shot (99.99%) were prepared with a molar ratio of Ta: Co: Te = 1: 1: 2 and sealed in a quartz tube under high vacuum. Then it was placed in a horizon two-zone tube furnace and maintained under a temperature gradient of 950–850 °C. After 2 weeks, shiny single crystals with a typical size of about $1 \times 2 \times 0.1$ mm^3 were obtained. The structure of the crystals was characterized by X-ray diffraction with Cu Ka radiation at room temperature using a Rigaku Miniex diffractometer. The diffraction pattern can be well indexed by the (00l) reflections. Magnetic measurements were performed using the QD Magnetic Property Measurement System (MPMS) with the Vibrating Sample Magnetometer (VSM) mode. Temperature-dependent magnetic susceptibility and the field-dependent magnetization results were collected with an external magnetic field of 0.2 T, which is parallel to the c axis.

ARPES measurement

ARPES measurements were performed at the beamline 13U of the National Synchrotron Radiation Laboratory (NSRL) and the beamline 1 of the Hiroshima Synchrotron Radiation Center (HSRC), Hiroshima, Japan. The energy resolution was set at 25 meV for Fermi surface mapping and 12.5 meV for band structure measurements, respectively. The angular resolution was set at 0.1°. Samples were cleaved in situ along the (001) crystal plane under ultra-high vacuum with pressure better than 5×10^{-11} mbar and temperatures around 20 K.

First-principles calculations

The first-principles calculations are performed using the Vienna ab initio simulation package[44,45] within the projector augmented wave method[46]. The exchange correlation functional was treated within the generalized gradient approximation in the Perdew–Burke–Ernzerhof formalism[47]. The plane-wave basis with an energy cutoff of 500 eV. The BZ was sampled by using the Γ-centered 5×5×2 Monkhorst-Pack grid[48] in the self-consistent calculation. The spin polarized calculations

are calculated to give a nonmagnetic ground state. In addition, a tight-binding (TB) Hamiltonian based on the maximally localized Wannier functions (MLWF)[49] is constructed by using the Wannier90 package[50]. Through the TB Hamiltonian, the Fermi surface is further plotted by using the WannierTools package[51].

DATA AVAILABILITY
The data that support the findings of this study are available from the corresponding authors upon reasonable request.

REFERENCES

1. Novoselov, K. S. et al. Two-dimensional gas of massless Dirac fermions in graphene. *Nature* **438**, 197–200 (2005).
2. Novoselov, K. S. et al. Electric field effect in atomically thin carbon films. *Science* **306**, 666–669 (2004).
3. Hsieh, D. et al. A topological Dirac insulator in a quantum spin Hall phase. *Nature* **452**, 970–974 (2008).
4. Chen, Y. L. et al. Experimental realization of a three-dimensional topological insulator, Bi$_2$Te$_3$. *Science* **325**, 178–181 (2009).
5. Hsieh, D. et al. A tunable topological insulator in the spin helical Dirac transport regime. *Nature* **460**, 1101–1105 (2009).
6. Xia, Y. et al. Observation of a large-gap topological-insulator class with a single Dirac cone on the surface. *Nat. Phys.* **5**, 398–402 (2009).
7. Lv, B. Q. et al. Observation of Weyl nodes in TaAs. *Nat. Phys.* **11**, 724–727 (2015).
8. Xu, S. Y. et al. Discovery of a Weyl fermion state with Fermi arcs in niobium arsenide. *Nat. Phys.* **11**, 748–754 (2015).
9. Xu, S. Y. et al. Discovery of a Weyl fermion semimetal and topological Fermi arcs. *Science* **349**, 613–617 (2015).
10. Xu, S. Y. et al. Observation of Fermi arc surface states in a topological metal. *Science* **347**, 294–298 (2015).
11. Yang, L. X. et al. Weyl semimetal phase in the non-centrosymmetric compound TaAs. *Nat. Phys.* **11**, 728–732 (2015).
12. Liu, Z. K. et al. A stable three-dimensional topological Dirac semimetal Cd$_3$As$_2$. *Nat. Mater.* **13**, 677–681 (2014).
13. Liu, Z. K. et al. Discovery of a three-dimensional topological Dirac semimetal, Na$_3$Bi. *Science* **343**, 864–867 (2014).
14. Alexandradinata, A., Wang, Z. & Bernevig, B. A. Topological insulators from group cohomology. *Phys. Rev. X* **6**, 021008 (2016).
15. Bradlyn, B. et al. Beyond Dirac and Weyl fermions: unconventional quasiparticles in conventional crystals. *Science* **353**, aaf5037 (2016).
16. Huang, S. M. et al. New type of Weyl semimetal with quadratic double Weyl fermions. *Proc. Natl Acad. Sci. USA* **113**, 1180–1185 (2016).
17. Wang, Z., Alexandradinata, A., Cava, R. J. & Bernevig, B. A. Hourglass fermions. *Nature* **532**, 189–194 (2016).
18. Weng, H., Fang, C., Fang, Z. & Dai, X. Topological semimetals with triply degenerate nodal points in θ-phase tantalum nitride. *Phys. Rev. B* **93**, 241202 (2016).
19. Wieder, B. J., Kim, Y., Rappe, A. M. & Kane, C. L. Double Dirac semimetals in three dimensions. *Phys. Rev. Lett.* **116**, 186402 (2016).
20. Zhu, Z., Winkler, G. W., Wu, Q., Li, J. & Soluyanov, A. A. Triple point topological metals. *Phys. Rev. X* **6**, 031003 (2016).
21. Liu, Q. & Zunger, A. Predicted realization of cubic Dirac fermion in quasi-one-dimensional transition-metal monochalcogenides. *Phys. Rev. X* **7**, 021019 (2017).
22. Wieder, B. J. et al. Wallpaper fermions and the nonsymmorphic Dirac insulator. *Science* **361**, 246–251 (2018).
23. Wu, W., Yu, Z. M., Zhou, X., Zhao, Y. X. & Yang, S. A. Higher-order Dirac fermions in three dimensions. *Phys. Rev. B* **101**, 205134 (2020).
24. Guo, P. J., Wei, Y. W., Liu, K., Liu, Z. X. & Lu, Z. Y. Eightfold degenerate fermions in two dimensions. *Phys. Rev. Lett.* **127**, 176401 (2021).
25. Cano, J., Bradlyn, B. & Vergniory, M. G. Multifold nodal points in magnetic materials. *APL Mater.* **7**, 101125 (2019).
26. Schoop, L. M. et al. Tunable Weyl and Dirac states in the nonsymmorphic compound CeSbTe. *Sci. Adv.* **4**, eaar2317 (2018).
27. Xu, C. Z. et al. Elemental topological Dirac semimetal: α-Sn on InSb(111). *Phys. Rev. Lett.* **118**, 146402 (2017).
28. Kumar, N. et al. Signatures of sixfold degenerate exotic fermions in a superconducting metal PdSb$_2$. *Adv. Mater.* **32**, e1906046 (2020).
29. Sun, Z. P. et al. Direct observation of sixfold exotic fermions in the pyrite-structured topological semimetal PdSb$_2$. *Phys. Rev. B* **101**, 155114 (2020).

30. Yáng, X. et al. Observation of sixfold degenerate fermions in PdSb₂. *Phys. Rev. B* **101**, 201105 (2020).

31. Chapai, R. et al. Superconducting properties of the spin Hall candidate Ta₃Sb with eightfold degeneracy. *Phys. Rev. B* **105**, 184510 (2022).

32. Zhang, X. et al. Eightfold fermionic excitation in a charge density wave compound. *Phys. Rev. B* **102**, 035125 (2020).

33. Berry, T., Pressley, L. A., Phelan, W. A., Tran, T. T. & McQueen, T. M. Laser-enhanced single crystal growth of non-symmorphic materials: applications to an eight-fold fermion candidate. *Chem. Mater.* **32**, 5827–5834 (2020).

34. Yuan, N. F. Q., Isobe, H. & Fu, L. Magic of high-order van Hove singularity. *Nat. Commun.* **10**, 5769 (2019).

35. Yuan, N. F. Q. & Fu, L. Classification of critical points in energy bands based on topology, scaling, and symmetry. *Phys. Rev. B* **101**, 125120 (2020).

36. Singha, R. et al. TaCo₂Te₂: an air-stable, high mobility Van der Waals material with probable magnetic order. *Adv. Funct. Mater.* **32**, 2108920 (2021).

37. Wang, Q. et al. Large intrinsic anomalous Hall effect in half-metallic ferromagnet Co₃Sn₂S₂ with magnetic Weyl fermions. *Nat. Commun.* **9**, 3681 (2018).

38. Liu, E. et al. Giant anomalous Hall effect in a ferromagnetic Kagome-lattice semimetal. *Nat. Phys.* **14**, 1125–1131 (2018).

39. Bilbao Crystallographic Server. https://www.cryst.ehu.es/ (2023).

40. Ma, J. et al. Experimental evidence of hourglass fermion in the candidate non-symmorphic topological insulator KHgSb. *Sci. Adv.* **3**, e1602415 (2017).

41. Wang, L., Jian, S.-K. & Yao, H. Hourglass semimetals with nonsymmorphic symmetries in three dimensions. *Phys. Rev. B* **96**, 075110 (2017).

42. Li, S. et al. Nonsymmorphic-symmetry-protected hourglass Dirac loop, nodal line, and Dirac point in bulk and monolayer X₃SiTe₆ (X = Ta, Nb). *Phys. Rev. B* **97**, 045131 (2018).

43. Weng, H. et al. Topological node-line semimetal in three-dimensional graphene networks. *Phys. Rev. B* **92**, 045108 (2015).

44. Kresse, G. & Furthmüller, J. Efficient iterative schemes for ab initio total-energy calculations using a plane-wave basis set. *Phys. Rev. B* **54**, 11169 (1996).

45. Kresse, G. & Joubert, D. From ultrasoft pseudopotentials to the projector augmented-wave method. *Phys. Rev. B* **59**, 1758 (1999).

46. Blöchl, P. E. Projector augmented-wave method. *Phys. Rev. B* **50**, 17953 (1994).

47. Perdew, J. P., Burke, K. & Ernzerhof, M. Generalized gradient approximation made simple. *Phys. Rev. Lett.* **77**, 3865 (1996).

48. Monkhorst, H. J. & Pack, J. D. Special points for Brillouin-zone integrations. *Phys. Rev. B* **13**, 5188 (1976).

49. Souza, I., Marzari, N. & Vanderbilt, D. Maximally localized Wannier functions for entangled energy bands. *Phys. Rev. B* **65**, 035109 (2001).

50. Pizzi, G. et al. Wannier90 as a community code: new features and applications. *J. Phys. Condens. Matter* **32**, 165902 (2020).

51. Wu, Q., Zhang, S., Song, H.-F., Troyer, M. & Soluyanov, A. A. WannierTools: an open-source software package for novel topological materials. *Comput. Phys. Commun.* **224**, 405 (2018).

52. Deng, K. et al. Experimental observation of topological Fermi arcs in type-II Weyl semimetal MoTe₂. *Nat. Phys.* **12**, 1105–1110 (2016).

53. Huang, L. et al. Spectroscopic evidence for a type II Weyl semimetallic state in MoTe₂. *Nat. Mater.* **15**, 1155–1160 (2016).

54. Jiang, J. et al. Signature of type-II Weyl semimetal phase in MoTe₂. *Nat. Commun.* **8**, 13973 (2017).

55. Xu, S. Y. et al. Discovery of Lorentz-violating type II Weyl fermions in LaAlGe. *Sci. Adv.* **3**, e1603266 (2017).

56. Belopolski, I. et al. Signatures of a time-reversal symmetric Weyl semimetal with only four Weyl points. *Nat. Commun.* **8**, 942 (2017).

57. Borisenko, S. et al. Time-reversal symmetry breaking type-II Weyl state in YbMnBi₂. *Nat. Commun.* **10**, 3424 (2019).

58. Belopolski, I. et al. Discovery of topological Weyl fermion lines and drumhead surface states in a room temperature magnet. *Science* **365**, 1278–1281 (2019).

59. Liu, D. F. et al. Magnetic Weyl semimetal phase in a Kagomé crystal. *Science* **365**, 1282–1285 (2019).

60. Lv, B. Q. et al. Observation of three-component fermions in the topological semimetal molybdenum phosphide. *Nature* **546**, 627–631 (2017).

61. Ma, J. Z. et al. Three-component fermions with surface Fermi arcs in tungsten carbide. *Nat. Phys.* **14**, 349–354 (2018).

62. Li, Y. et al. Topological origin of the type-II Dirac fermions in PtSe₂. *Phys. Rev. Mater.* **1**, 074202 (2017).

63. Zhang, K. et al. Experimental evidence for type-II Dirac semimetal in PtSe₂. *Phys. Rev. B* **96**, 125102 (2017).

64. Bahramy, M. S. et al. Ubiquitous formation of bulk Dirac cones and topological surface states from a single orbital manifold in transition-metal dichalcogenides. *Nat. Mater.* **17**, 21–28 (2018).

65. Fei, F. et al. Nontrivial Berry phase and type-II Dirac transport in the layered material PdTe₂. *Phys. Rev. B* **96**, 041201 (2017).

66. Noh, H. J. et al. Experimental realization of type-II Dirac fermions in a PdTe₂ Superconductor. *Phys. Rev. Lett.* **119**, 016401 (2017).

67. Yan, M. et al. Lorentz-violating type-II Dirac fermions in transition metal dichalcogenide PtTe₂. *Nat. Commun.* **8**, 257 (2017).

68. Miao, H. et al. Observation of double Weyl phonons in parity-breaking FeSi. *Phys. Rev. Lett.* **121**, 035302 (2018).

69. Rao, Z. et al. Observation of unconventional chiral fermions with long Fermi arcs in CoSi. *Nature* **567**, 496–499 (2019).

70. Sanchez, D. S. et al. Topological chiral crystals with helicoid-arc quantum states. *Nature* **567**, 500–505 (2019).

71. Schröter, N. B. M. et al. Chiral topological semimetal with multifold band crossings and long Fermi arcs. *Nat. Phys.* **15**, 759–765 (2019).

72. Takane, D. et al. Observation of chiral fermions with a large topological charge and associated Fermi-arc surface states in CoSi. *Phys. Rev. Lett.* **122**, 076402 (2019).

73. Schroter, N. B. M. et al. Observation and control of maximal Chern numbers in a chiral topological semimetal. *Science* **369**, 179–183 (2020).

74. Lv, B. Q. et al. Observation of multiple types of topological fermions in PdBiSe. *Phys. Rev. B* **99**, 241104 (2019).

ACKNOWLEDGEMENTS

AUTHOR CONTRIBUTIONS

C.C. and H.R. conceived the project. ARPES measurements were performed by H.R., S.K., F.Z., C.Z., Y.W., Z.H., Y.C., C.L., X.M., and K.S. with the assistance of Y.L. and S.C. Density functional theory calculations were performed by Z.H., Q.W., and H.X. Sample growth and characterization were performed by X.Z., L.W., S.G., B.S., J.L., Y.Y., and Z.W. All authors contributed to the manuscript.

COMPETING INTERESTS

The authors declare no competing interests.

ADDITIONAL INFORMATION

Supplementary information The online version contains supplementary material available at https://doi.org/10.1038/s41535-023-00565-8.

Correspondence and requests for materials should be addressed to Zhiwei Wang, Hu Xu or Chaoyu Chen.

Reprints and permission information is available at http://www.nature.com/reprints

Publisher's note Springer Nature remains neutral with regard to jurisdictional claims in published maps and institutional affiliations.